Intrinsic anharmonicity and thermal properties of ultralow thermal conductivity math xmlns="http://www.w3.org/1998/Math/MathML">mrow>msub>mi>Ba/mi>mn>6/mn>/msub>msub>mi>Sn/mi>mn>6/mn>/msub>msub>mi>Se/mi>mn>13/mn>/msub>/mrow>/math>

Wilarachchige D. C. B. Gunatilleke, Rinkle Juneja, Oluwagbemiga P. Ojo, Andrew F. May, Hsin Wang, Lucas Lindsay, and George S. Nolas

Phys. Rev. Materials **5**, 085002 — Published 5 August 2021

DOI: 10.1103/PhysRevMaterials.5.085002

Intrinsic Anharmonicity and Thermal Properties of Ultralow Thermal Conductivity $Ba_6Sn_6Se_{13}$

Wilarachchige D. C. B. Gunatilleke[1], Rinkle Juneja[2], Oluwagbemiga P. Ojo[1], Andrew F. May[2], Hsin Wang[2], Lucas Lindsay[2], and George S. Nolas[1*]

[1] *Department of Physics, University of South Florida, Tampa, FL, 33620, USA*

[2] *Materials Science and Technology Division, Oak Ridge National Laboratory, Oak Ridge, TN, 37831, USA*

Abstract

Ultralow thermal conductivity materials continue to be of great interest for technologically important applications such as thermal insulators and thermoelectrics. Often, such materials possess constituents with extensive dynamic disorder, or "rattlers", or structural disorder such as metallic glasses. Nevertheless, targeted crystalline bonding order and anharmonicity can provide effective means for scattering of the phonons in certain materials. Our combined experimental and theoretical investigation of $Ba_6Sn_6Se_{13}$ reveal such a material, with ultralow thermal conductivity measured over a large temperature range. Optic phonon modes hybridize with acoustic modes at relatively low energies resulting in strong acoustic-optic scattering and limited phonon lifetimes. Moreover, our investigations reveal various avoided crossings at low energies that contribute to phonon scattering. These are derived from chiral phase symmetries and may result in nontrivial topological behaviors for phonon band crossings in this chiral material. This work contributes to the ongoing research on low thermal conductivity materials and the underlying mechanisms that affect their thermal behaviors. Manipulation of these effects may provide pathways for enhancement of material properties for targeted thermal applications using similar materials.

Introduction

The search for new materials that possess low thermal conductivity, κ, continues to be of keen interest for technologically relevant applications. Thermal barrier coating materials require low κ in order to protect the underlying substrate, while it is essential in limiting the heating that occurs during operation in rewritable devices that are based on phase change systems.[1-4] For the case of thermal management devices, such as thermoelectrics, a low κ is required in order to obtain maximum performance.[5-11] For certain applications, disordered or amorphous materials have also been utilized as they typically possess low κ values over relatively large temperature ranges due to the non-periodicity of their crystal structures. For all of these examples, an understanding of the basic mechanisms that govern low κ is essential. Building on Slack's efforts to describe crystalline κ from simple material parameters (e.g., unit cell complexity, atomic masses, Debye temperature, θ_D),[12] more sophisticated models have been developed to probe and understand the low κ limit.[13-15] These approaches extend beyond direct phonon transport, nevertheless anharmonicity from specific structural features, for example lattice instabilities and stereochemically active lone-pair electrons, still play an important role in determining low κ derived from vibrational dynamics and transport in materials.[16-21] When combined with other attributes, such as large and complex crystal structures and low sound velocities, materials with very low κ values can be realized.

Transition and main-group-metal chalcogenides is one family of compounds that exhibit the chemical and physical properties relevant to possessing low κ values.[1, 5, 7, 22-29] Ternary chalcogenides with non-toxic and primarily earth abundant elements form a group of materials of current interest. Motivated by these material types and understanding the underlying mechanisms that govern their observed low κ behaviors, we have experimentally and theoretically investigated the thermal properties of $Ba_6Sn_6Se_{13}$. The crystal and electronic structures of this relatively large bandgap material (1.5 eV) have been previously described[30]; $Ba_6Sn_6Se_{13}$ contains lone pair electrons as well as different valences of tin cations (Sn^{2+}/Sn^{4+}), both known to result in strong phonon anharmonicity. The scattering of phonons in $Ba_6Sn_6Se_{13}$ is further enduced by structural complexity and a large number of atoms per unit cell, which give rise to numerous low energy optic branches that provide scattering channels for the heat-carrying acoustic phonons. The complex overlapping phonon band structure (demonstrated below) can potentially drive non-phonon vibrational transport that has been highlighted by recent theoretical and experimental

efforts in complex unit cell crystals.[14-15] Moreover, the presence of chiral structural symmetry in this non-symmorphic material leads to phonon bands with varying quasiangular momenta that governs various phonon band crossings and anticrossings of relevance to scattering and transport.

Experimental Details

We synthesized $Ba_6Sn_6Se_{13}$ following an approach that is similar to that of previously reported in Feng *et al*.[30] Powder X-ray diffraction data, collected in Bragg-Bretano geometry using a Bruker D8 Focus Diffractometer, a graphite monochromator and CuKα (1.54056 Å) radiation, were analyzed by Rietveld refinement using GSAS II[31]. Details on processing and our structural characterization results can be found in the Supplemental Information[32]. Low temperature thermal transport measurements on a 2x2x5 mm^3 parallelepiped were accomplished with two different apparatuses, a custom-designed radiation shielded vacuum probe with an 8% maximum experimental uncertainty[33,34] and Quantum Design Physical Properties Measurement system (PPMS). We calibrated κ measurements from our PPMS by measurements from our custom-built system. Above room temperature, laser flash thermal diffusivity measurements were conducted on a 1 mm thick disc using a NETZSCH LFA475 system under flowing Ar with an experimental uncertainty of 5%. The relationship $\kappa = DdC_V$ was used to determine κ, where D is the measured thermal diffusivity, d is the measured density, and C_V is the specific heat at constant volume estimated via the Dulong-Petit limit. Specific heat at constant pressure, C_P, measurements below room temperature were performed using the PPMS with Apiezon N-grease and appropriate addenda.

Phonon calculations were carried out using first-principles density functional theory[35, 36] as implemented in the Vienna Ab initio Simulation Package (VASP)[37, 38] and using the lattice parameters and atomic positions reported in reference 30. Calculations were based on the local density approximation[39] with projector augmented wave potentials[40, 41]. Harmonic interatomic force constants (IFCs) for determining phonon properties were obtained from finite-difference supercell calculations as implemented in PHONOPY[42]. A supercell of 2x2x1 (400 atoms), Γ-point-only sampling, energy cut-off of 600 eV, and energy convergence threshold of 10^{-8} eV were used. Non-analytic polar corrections proposed by Gonze et al.[43, 44] were included in the phonon calculations, except for the chiral dispersion described below. To assess the bonding behaviour in

$Ba_6Sn_6Se_{13}$, the electron localization function (ELF)[45-47] was calculated for the unit cell using a 2x2x1 *k*-mesh and the same convergence parameters as described above.

Results and Discussion

Complex unit cell systems with a large number of degrees of freedom, such as $Ba_6Sn_6Se_{13}$, present significant numerical challenges when computing κ, which was not explicitly calculated here. Nevertheless, significant insights can be gained from the underlying harmonic properties, such as frequencies and velocities, which are accessible to density functional theory calculation, though not without their own challenges. Figure 1(a) shows the phonon dispersion of $Ba_6Sn_6Se_{13}$ along various high-symmetry directions. The absence of imaginary modes, i.e. negative frequency phonons, indicates the dynamical stability of this material. The total frequency span and nature of the phonon branches, such as the presence of frequency gaps, can be correlated with our experimental κ data described below[48, 49]. In $Ba_6Sn_6Se_{13}$ the energy span of the phonon modes is relatively small (less than 32 meV) with a very large number of low frequency optic branches that are anticipated to result in increased scattering of heat-carrying acoustic phonons and thus low κ. Furthermore, the optic branches hybridize with the acoustic modes below 3 meV, which can also cause strong acoustic-optic scattering and shorter phonon lifetimes (τ). Since $\kappa \sim C_V v^2 \tau$, where v is phonon velocity, short lifetimes and lower velocity phonons lead to lower κ. We projected the calculated mode group velocities on the phonon dispersion in Figure 1(a). The projected color scale for the calculated velocities is normalized by the highest calculated velocity, 2883 m/s, for a longitudinal acoustic (LA) mode along the Γ-*Y* direction. Unsurprisingly, the acoustic branches possess generally larger velocities relative to the predominant optic modes; however, a small subset of optic modes near the *Z* point also have relatively large velocities. We therefore expect that the phonons below ~3 meV carry most of the heat in $Ba_6Sn_6Se_{13}$. Figure 1(b) shows the partial phonon density of states (PDOS) for each atom. All atoms give significant contributions to the low-energy regime owing to the heavy atomic masses of Ba and Sn and the large number of lighter Se atoms. In Figure 1(b) the PDOS for Sn atoms with different valences (Sn^{2+} and Sn^{4+}) are differentiated, and the Sn^{2+} atoms (the shaded yellow regions in the figure) are found to give significant contributions to the PDOS at low energies. The valence of tin will be of particular importance in understanding the thermal properties of $Ba_6Sn_6Se_{13}$, as described below.

Knowledge of the vibrational heat capacity can provide insight into κ. Figure 2 shows our measured temperature-dependent C_p data as well as our calculations for C_v. In Figure 2(a) C_p and C_v are normalized by $3RN$, where R is the specific gas constant and N is the number of atoms in the formula unit. The calculated C_v is smaller than the measured C_p, particularly at higher temperatures where anharmonic effects become more important and add to C_p. In the intermediate-temperature range, C_p and C_v deviate from the behaviour expected for Debye-like acoustic phonons, as shown in Figure 2(b). In particular, C/T^3 versus T shows a peak near 10 K for both, presumably due to the influence of low-velocity optical modes. This peak can be related to contributions of these Einstein modes at approximately 1/5 of a characteristic Einstein temperature. As described above, the top of the acoustic band is near 3 meV, or approximately 35 K, above which the low-velocity phonons, or more Einstein-like phonons, start to dominate. This is in-line with the estimated effective Einstein temperature of 48 K obtained from the data shown in Figure 2(b).

The Debye temperature, θ_D, can be obtained from our experimental data using the low-temperature (T) limit of the Debye model, $C_P = \gamma T + \beta T^3$, where γT is the electronic contribution, found to be negligible as expected for this relatively large bandgap material. The lattice contribution βT^3 is related to the Debye temperature by $\theta_D = (12\pi RN/5\beta)^{1/3}$. The fitted data are shown in Figure 2(c) and result in θ_D = 166 K. A similar computation from our calculated C_v resulted in θ_D = 160 K. It is instructive to also estimate θ_D from the calculated group velocities using the expression $\theta_D = \frac{\hbar}{k_B} v_D \sqrt[3]{\frac{6\pi^2 N}{V}}$, where V is the unit cell volume (3.10 x 10^{-27} m^3) and N is the number of atoms in the unit cell (100)[50]. The Debye frequency, v_D, can be estimated from $v_D^{-3} = \frac{1}{3}(v_{LA}^{-3} + v_{TA1}^{-3} + v_{TA2}^{-3})$, where v_{LA} and v_{TA} are longitudinal and transverse sound velocities averaged over all high-symmetry directions, respectively, with v_{LA} = 2856 m/s, v_{TA1} = 1658 m/s, and v_{TA2} = 1895 m/s. This analysis results in θ_D = 184 K, a value that is in reasonable agreement with those obtained from C_p and C_v.

The presence of low valence Sn^{2+} in $Ba_6Sn_6Se_{13}$ may also lead to formation of lone electron pairs and anisotropic bonding. To analyse the bonding attributes, we calculated the electron localization function (ELF), which quantifies the probability density of same spin electron pairs[45-47]. The

calculated ELF is projected onto a color scale in Figure 3, where ELF = 1 and 0 correspond to high and low charge densities, respectively. Consistent with the different valence states, the low (Sn^{2+}) and high (Sn^{4+}) valence tin atoms result in high and low electron densities around them, respectively, as shown along (100) planes in Figure 3. The higher valence Sn^{4+} atoms occupy tetrahedral sites ($Sn^{4+}Se_4$) with a delocalized charge density around them. This is in accordance with the atomic configuration of Sn; however, the lower valence Sn^{2+} are bonded with 3 Se atoms and hence allow for the formation of lone pair electrons. The high electron density around the lone pair is illustrated along (100) planes as well as along a combination of (001) and (010) planes. The presence of lone pairs and anisotropic bonding have been correlated with low κ in other materials [51-57]. In $Ba_6Sn_6Se_{13}$, five out of six tin atoms are involved with lone-pair bonds and, as shown in Figure 1(b), these Sn^{2+} contribute strongly to the PDOS at low energies. This will have strong influence on the vibrational properties and κ of $Ba_6Sn_6Se_{13}$.

Figure 4 shows the measured temperature-dependent κ data for $Ba_6Sn_6Se_{13}$ over a large temperature range. The excellent agreement between the high (300 to 675 K) and low (4 to 300 K) temperature κ data, measured on two different pieces of the polycrystalline material with different dimensions, is an indication of the homogeneity of the specimen prepared for this investigation. For this relatively large bandgap material the electronic contributions to κ over the entire measured temperature range is expected to be negligible. As shown in Figure 4, ultralow κ values were observed over a large temperature range, with κ = 0.18 $Wm^{-1}K^{-1}$ at room temperature. Although the general features of the temperature dependence of κ are typical of crystalline dielectrics, with a maximum at low T that is a function of θ_D, $T_{max} \sim \theta_D$ /10, the weak T-dependence in addition to the ultralow κ for $T > T_{max}$ may be an indication of non-phonon transport in addition to the scattering mechanisms described above that limit phonon-mediated transport.

In complex anharmonic crystals with low κ, similar to that of $Ba_6Sn_6Se_{13}$ here, recent literature suggests that vibrational thermal transport cannot be simply characterized by phonons[14, 15, 58]. In such materials, closely spaced phonon bands are broadened due to anharmonic scattering or various types of disorder, which leads to band overlap and exchange of thermal energy among them, allowing for 'diffusion-like, non-phonon' transport[15, 59-61]. Furthermore, strong anharmonic scattering has been shown to limit phonon mean free paths below the average interatomic spacing

of complex crystals, particularly for optic phonons with small group velocities.[14] Such phonons are not well-defined, and their thermal energy transport has been described by minimum κ models.[13, 14] As the complexity of $Ba_6Sn_6Se_{13}$ precludes full anharmonic calculations of the vibrational lifetimes to fully assess these possibilities, here we build a description of thermal transport based on classical models for phonon scattering and minimum κ informed by DFT-derived harmonic properties of each phonon with wavevector $\vec{q}$ and polarization *j*: frequencies ($\omega_{\vec{q}j}$), mode specific heats ($C_{\vec{q}j}$), and velocities ($\vec{v}_{\vec{q}j}$).

To model κ of $Ba_6Sn_6Se_{13}$ we divide the phonons into two frequency regions: those with frequencies below 4 meV (acoustic modes and low frequency optic modes) and optic modes with frequencies above 4 meV (majority of optic modes in this material). Below 4 meV, the phonons are assumed to behave like typical phonons with reasonable mean free paths as supported by relatively large velocities compared with the majority of higher frequency optic modes (see Figure 1). Above 4 meV, the phonons have significant overlap, many available scattering channels, and low velocities, all of which restrict their mean free paths, which we model to be on the order of the average interatomic lattice spacing, l = 2.88 Å.

For phonons with frequencies below 4 meV we assume the scattering rate model[62-65]:

$$1/\tau_{\vec{q}j} = |\vec{v}_{\vec{q}j}|/L + A\omega_{\vec{q}j}^4 + B\omega_{\vec{q}j}^2 T e^{-\theta_D/3T} \qquad (1)$$

where the first, second, and third terms on the right-hand side correspond to boundary, point defect, and anharmonic resistances, respectively. Here $|\vec{v}_{\vec{q}j}|$ is the mode speed averaged over Cartesian directions and L=70 nm was fit to the lowest temperature measured κ data in Figure 4. In addition, $A = 3.46 \times 10^{-41}$ s^3 and $B = 2.86 \times 10^{-17}$ sK^{-1} are parameters adjusted to fit the peak κ at T = 30 K and the high temperature κ, respectively. Though not independent, these parameters were not strongly correlated in the fitting process. The calculated θ_D = 160 K was used here. The lifetimes determined by Equation 1 are used in:

$$\kappa_{\omega<4\text{meV}} = \sum_{\vec{q}j} C_{\vec{q}j} \, | v_{\vec{q}j}^2 | \, \tau_{\vec{q}j} \qquad (2)$$

where $| v_{\vec{q}j}^2 |$ is the average of the velocity squared along three Cartesian directions. For phonons with frequencies above 4 meV we assume the scattering mechanisms are strong enough to restrict phonons to mean free paths on the order of the interatomic spacing, i.e., minimum κ limit.[13, 14]. In this case, we define the thermal conductivity contribution from these modes as:

$$\kappa_{\omega\geq4\text{meV}} = \sum_{\vec{q}j} C_{\vec{q}j} \, | v_{\vec{q}j} | \, l \qquad (3)$$

Contributions from phonons of both frequency regions are combined to give the total $\kappa = \kappa_{\omega<4\text{meV}} + \kappa_{\omega\geq4\text{meV}}$, which is shown in Figure 4, as well as their separate contributions.

This model gives a reasonable description of the temperature-dependent behavior of κ in $Ba_6Sn_6Se_{13}$ in the low and high temperature regimes. At intermediate temperatures 100 K < *T* < 300 K the model does not account for the relatively weak measured temperature-dependence of κ. Agreement of measured and modeled low temperature κ behavior demonstrates that transport is governed by phonon-grain boundary scattering in this temperature regime. However, the prediction of ultrasmall grain sizes should not be taken seriously as the model lacks sophisticated description of phonon-boundary interactions.

The underlying structure that dictates the bonding and vibrational properties of $Ba_6Sn_6Se_{13}$ has the interesting aspect of being chiral (space group $P2_12_12_1$), thus, it lacks inversion symmetry with the possibility of hosting topological quasiparticle features[66]. In addition, the screw symmetry allows a twisting dynamical description along the (0, 0, *z*) chiral axis. The quasiparticle dynamics of the full 100 atom unit cell can therefore be described in terms of the interactions of 50 atoms related to the other 50 by a rotation of π and a translation of *c*/2 along the chiral axis, with *c* being a lattice constant. In terms of phonons, the dynamical matrix of a chiral system is[67, 68]

$$D_{\alpha\beta}^{kk'}(q_z l) = \frac{1}{\sqrt{m_k m_{k'}}} \sum_{h'\delta} \Phi_{\alpha\delta}^{0k,p'h'k'} S(\pi n_{h'})_{\delta\beta} e^{il\pi n_{h'}} e^{iq_z c/2} \, , \qquad (4)$$

where m_k is the mass of the k atom, the Greek letters represent Cartesian directions, $\Phi_{\alpha\delta}^{0k,p'h'k'}$ are harmonic force constants between atom k in the smaller 50 atom unit cell with k' in the p' unit cell in the h' layer along the chiral axis, and $S(\pi n_h)_{\alpha\beta}$ is a rotation operator with n_h an integer labeling the layer. In Equation 4, q_z is the continuous translational momentum along the z axis and l is a quantum number reminiscent of a quasiangular momentum derived from the screw symmetry of the chiral crystal. The rotational phase factors in Equation 4, $e^{il\pi n_h}$, also enter the scattering matrix elements among quasiparticles (for example three-phonon and electron-phonon interactions) that lead to phase interference and conservation of l [67, 68]. These rotational phase factors are also associated with symmetry-enforced crossings and band topology.

Figure 5 shows the low frequency dispersion of $Ba_6Sn_6Se_{13}$ along the (0, 0, z) chiral axis with blue and red curves corresponding to quasiangular momenta $l = 0$ and $l = 1$, respectively. We note that this dispersion, derived from Equation 4, is exactly the same as that from a traditional 'non-chiral' dynamical description (see Figure 1(a), with polar corrections in that case). This highlights the underlying symmetry of the quasiparticles. The two half Brillouin zones are shown in the figure to demonstrate the periodicity of the rotational phases. At the Brillouin zone boundary, each mode has a conjugate partner and thus symmetry-enforced crossing of branches with opposite slope occur. It is important to note that bands carrying the same quasiangular momentum cannot cross, and this leads to various avoided crossings in the dispersion of $Ba_6Sn_6Se_{13}$ (see Figure 5). Therefore, materials with these symmetry elements possess avoided crossings that can be understood from the perspective of shared quantum phase symmetry. Although the rotational phases alternate from zone to zone, the avoided crossings are conserved. To the best of our knowledge, this chiral behavior has not been previously reported for this material. With regard to the effect on the thermal properties of $Ba_6Sn_6Se_{13}$, avoided crossings have been reported to be responsible for low κ in other materials,[52, 53, 69, 70] and may contribute to the ultralow κ measured for $Ba_6Sn_6Se_{13}$ here.

Conclusions

We investigated the thermal properties of $Ba_6Sn_6Se_{13}$ with a combined experimental and theoretical effort. Specifically, we synthesized and mesaured the temperature-dependent specific heat capacity and thermal conductivity of this material and employed first-principles simulations

of the phonon dispersion, PDOS, heat capacity, and ELF to identify the mechanisms that affect the vibrational modes and result in enhanced phonon scattering in this material. The ultralow κ over a relatively large temperature range stems from lone electron pairs and low phonon velocities. No scattering resistance from isolated ferroelectric soft modes was revealed from our analyses. Furthermore, many avoided crossings, that contribute to phonon scattering, can be understood from the underlying chiral symmetry that should be of interest for further investigations into this and other similar materials.

Acknowledgements

This work was supported by National Science Foundation Grant No. DMR-1748188. W.D.C.B.G and O.P.O. acknowledge the II-VI Foundation Block-Gift Program. H.W. acknowledges support of the Department of Energy Lightweight and Propulsion Materials program under the Vehicle Technologies Office. Specific heat measurements (A.F.M.) and phonon-related calculations (R.J. and L.L.) were supported by the U.S. Department of Energy, Office of Science, Basic Energy Sciences, Materials Science and Engineering Division. Oak Ridge National Laboratory is managed by UT-Battelle LLC under contract DE-AC05000OR22725. Computational resources were provided by the National Energy Research Scientific Computing Center (NERSC), a DOE Office of Science User Facility supported by the Office of Science of the US Department of Energy under Contract No. DE-AC02-05CH11231.

References

[1] D. R. Clarke and S. R. Phillpot, Thermal barrier coating materials, Mater. Today **8**, 22 (2005).

[2] M. Wuttig, and N. Yamada, Phase-change materials for rewriteable data storage, Nat. Mater. **6**, 824 (2007).

[3] C. L. Wan, W. Pan, Q. Xu, Y. X. Qin, J. D. Wang, Z. X. Qu, and M. H. Fang, Effect of point defects on the thermal transport properties of $(La_xGd_{1-x})_2Zr_2O_7$: Experiment and theoretical model, Phys. Rev. B **74**, 144109 (2006).

[4] T. Matsunaga, N. Yamada, R. Kojima, S. Shamoto, M. Sato, H. Tanida, T. Uruga, S. Kohara, M. Takada, P. Zalden, G. Bruns, I. Sergueev, H. C. Wille, R. P. Hermann, and M. Wuttig, Phase-change materials: vibrational softening upon crystallization and its impact on thermal properties, Adv. Funct. Mater. **21**, 2232 (2011).

[5] M. Beekman, D. T. Morelli, and G. S. Nolas, Better thermoelectrics through glass-like crystals, Nat. Mater. **14**, 1182 (2015).

[6] G. S. Nolas, and G. A. Slack, Thermoelectric clathrates: cagelike crystals may soon help to pump heat with electricity and to create electricity with heat, American Scientist **89**, 136 (2001).

[7] M. G. Kanatzidis, *The role of solid-state chemistry in the discovery of new thermoelectric materials*, in *Semiconductors and Semimetals*, edited by T. M. Trittt (Elsevier, San Diego, 2001) Vol. 69, p. 51-100.

[8] G. S. Nolas, J. Sharp, and H. J. Goldsmid, *Thermoelectrics: Basic Principles and New Materials Developments* (Springer-Verlag, Berlin, Germany 2001).

[9] L. D. Zhao, S. H. Lo, Y. Zhang, H. Sun, G. Tan, C. Uher, C. Wolverton, V. P. Dravid, and M. G. Kanatzidis, Ultralow thermal conductivity and high thermoelectric figure of merit in SnSe crystals, Nature **508**, 373 (2014)

[10] X. Lu, D. T. Morelli, Y. Xia, F. Zhou, V. Ozolins, H. Chi, X. Zhou, C. Uher, High performance thermoelectricity in earth- abundant compounds based on natural mineral tetrahedrites, Adv. Energy Mater. **3**, 342 (2013)

[11] H. Alam and S. Ramakrishna, A review on the enhancement of figure of merit from bulk to nano-thermoelectric materials, Nano Energy ***2***, 190 (2013).

[12] G. A. Slack, *Solid State Physics*, (Elsevier, Amsterdam, 1979) Vol. 34, p. 1-71.

[13] D. G. Cahill, S. K. Watson and R. O. Pohl, Lower limit to the thermal conductivity of disordered crystals, Phys. Rev. B **46**, 6131 (1992).

[14] S. Mukhopadhyay, D. S. Parker, B.C. Sales, A. A. Puretzky, M.A. McGuire and L. Lindsay, Two-channel model for ultralow thermal conductivity of crystalline Tl_3VSe_4, Science **360**, 1455 (2018).

[15] M. Simoncelli, N. Marzari, and F. Mauri, Unified theory of thermal transport in crystals and glasses, Nat. Phys. **15**, 809 (2019).

[16] T. Pandey, L. Lindsay, B. C. Sales, and D. S. Parker, Lattice instabilities and phonon thermal transport in TlBr, Phys. Rev. Mater. **4**, 045403 (2020).

[17] A. R. Khabibullin, K. Wei, T. D. Huan, G. S. Nolas and L. M. Woods, Compositional effects and electron lone-pair distortions in doped bournonites", Chem. Phys. Chem. **19**, 2635 (2018).

[18] E. J. Skoug and D. T. Morelli, Role of lone-pair electrons in producing minimum thermal conductivity in nitrogen-group chalcogenide compounds, Phys. Rev. Lett. **107**, 235901 (2011).

[19] M. D. Nielsen, V. Ozolins and J. P. Heremans, Lone pair electrons minimize lattice thermal conductivity, Energy Environ. Sci. **6**, 570 (2013).

[20] Y. Dong, A. R. Khabibullin, K. Wei, J. R. Salvador, G. S. Nolas, and L. M. Woods, Bournonite $PbCuSbS_3$: stereochemically active lone- pair Electrons that induce low thermal conductivity, Chem. Phys. Chem. **16**, 3264 (2015).

[21] D. Hobbis, K. Wei, H. Wang, J. Martin and G.S. Nolas, Synthesis, structure, Te alloying and physical properties of $CuSbS_2$, Inorg. Chem. **56**, 140404 (2017)

[22] M. Kwasi and J. A. Ibers. Rare-earth transition-metal chalcogenides, Chem. Rev. **102**, 1929 (2002).

[23] Y. Dong, H. Wang, and G. S. Nolas, Synthesis and thermoelectric properties of Cu excess $Cu_2ZnSnSe_4$, Phys. Status Solidi Rapid Res. Lett. **8**, 61 (2014).

[24] G. S. Nolas, S. M. Hassan, Y. Dong, and J. Martin, Synthesis, crystal structure and electrical properties of the tetrahedral quaternary chalcogenides CuM_2InTe_4 (M=Zn, Cd), J. Solid State Chem. **242**, 50 (2016).

[25] J. Li, S. Hao, S. Qu, C. Wolverton, J. Zhao, and Y. Wang, $In_4Pb_{5.5}Sb_5S_{19}$: A stable quaternary chalcogenide with low thermal conductivity, Inorg. Chem. **60**, 325 (2021).

[26] S. Roychowdhury, M. Samanta, S. Perumal, and K. Biswas, Germanium chalcogenide thermoelectrics: electronic structure modulation and low lattice thermal conductivity, Chem. Mater. **30**, 5799 (2018).

[27] R. Lefevre, D. Berthebaud, O. Perez, D. Pelloquin, S. Boudin, and F. Gascoin, Ultra-low thermal conductivity of $TlIn_5Se_8$ and structure of the new complex chalcogenide $Tl_{0.98}In_{13.12}Se_{16.7}Te_{2.3}$, J. Solid State Chem. **250**, 114 (2017).

[28] J. Kim, D. Chung, D. Bilc, S. Loo, J. Short, S. D. Mahanti, T. Hogan, and M. G. Kanatazidis, Crystal growth, thermoelectric properties, and electronic structure of $AgBi_3S_5$ and $AgSb_xBi_{3-x}S_5$ (x = 0.3)", Chem. Mater. **17**, 3606 (2005).

[29] Y. Jiang, F. Jia, L. Chen, and L-M Wu, $Cu_4Bi_4Se_9$: A thermoelectric symphony of rattling, anharmonic lone-pair, and structural complexity, ACS Appl. Mater. Interfaces **11**, 36616 (2019).

[30] K. Feng, X. Jiang, L. Kang, W. Yin, W. Hao, Z. Lin, J. Yao, Y. Wu, and C. Chen, $Ba_6Sn_6Se_{13}$: A new mixed valence selenostannate with NLO property", Dalton Trans. **42**, 13635 (2013).

[31] B. H. Toby, EXPGUI, a graphical user interface for GSAS, J. Appl. Cryst. **34**, 210 (2001).

[32] See Supplementary Material at [URL] for details on processing and structural characterization of $Ba_6Sn_6Se_{13}$.

[33] J. Martin, S. Erickson, G. S. Nolas, P. Alboni, T. M. Tritt, and J. Yang, Structural and transport properties of $Ba_8Ga_{16}Si_xGe_{30-x}$ clathrates, J. Appl. Phys. **99**, 044903 (2006).

[34] J. Martin, and G. S. Nolas, Apparatus for the measurement of electrical resistivity, Seebeck coefficient, and thermal conductivity of thermoelectric materials between 300 K and 12 K, Rev. Sci. Instrum. **87**, 015105 (2016).

[35] W. Kohn, and L. J. Sham, Self-consistent Equations including exchange and correlation effects, Phys. Rev.**140**, A1133 (1965).

[36] L. J. Sham, and M. Schlüter, Density-functional theory of the energy gap, Phys. Rev. Lett. **51**, 1888 (1983).

[37] G. Kresse, and J. Furthmüller, Efficient iterative schemes for ab initio total-energy calculations using a plane-wave basis set, Phys. Rev. B **54**, 11169 (1996).

[38] G. Kresse and J. Furthmüller, Efficiency of ab-initio total energy calculations for metals and semiconductors using a plane-wave basis set, Comput. Mater. Sci. **6**, 15 (1996).

[39] D. M. Ceperley and B. J. Alder, ground state of the electron gas by a stochastic method, Phys. Rev. Lett. **45**, 566 (1980).

[40] P. E. Blöchl, Projector Augmented-Wave Method, Phys. Rev. B**50**, 17953 (1994).

[41] G. Kresse and D. Joubert, From ultrasoft pseudopotentials to the projector augmented-wave method, Phys. Rev. B **59**, 1758 (1999).

[42] A. Togo and I. Tanaka, First principles phonon calculations in materials science, Scr. Mater. **108**, 1 (2015).

[43] X. Gonze, J.-C. Charlier, D. C. Allan, and M. P. Teter, Interatomic force constants from first principles: the case of α-quartz, Phys. Rev. B **17**, 13035 (1994).

[44] X. Gonze and C. Lee, Dynamical matrices, Born effective charges, dielectric permittivity tensors, and interatomic force constants from density-functional perturbation theory, Phys. Rev. B **55**, 10355 (1997).

[45] B. Silvi and A. Savin, Classification of chemical bonds based on topological analysis of electron localization functions, Nature **371**, 683 (1994).

[46] A. D. Becke and K. E. Edgecombe, A simple measure of electron localization in atomic and molecular systems, J. Chem. Phys. **92**, 5397 (1990).

[47] A. Savin, R. Nesper, S. Wengert, and T. F. Fässler, ELF: The electron localization function, Angew. Chem., Int. Ed. Engl. **36**, 1808 (1997).

[48] L. Lindsay, D. A. Broido, and T. L. Reinecke, Thermal conductivity and large isotope effect in GaN from first principles, Phys. Rev. Lett. **109**, 095901 (2012).

[49] R. Juneja, G. Yumnam, S. Satsangi, and A. K. Singh, Coupling the high-throughput property map to machine learning for predicting lattice thermal conductivity, Chem. Mater. **31**, 5145 (2019).

[50] C. Kittel, and P. McEuen, *Introduction to Solid State Physics* (Wiley, New York, 1976).

[51] S. Lee, K. Esfarjani, T. Luo, J. Zhou, Z. Tian, and G. Chen, "Resonant Bonding Leads to Low Lattice Thermal Conductivity" Nat. Commun. **5**, 3525 (2014).

[52] R. Juneja and A. K. Singh, Rattling-induced ultralow thermal conductivity leading to exceptional thermoelectric performance in $AgIn_5S_8$, ACS Appl. Mater. Interfaces **11**, 33894 (2019).

[53] S. Mukhopadhyay and T. L. Reinecke, Lone-pair electron-driven thermoelectrics at room temperature, J. Phys. Chem. Lett. **10**, 4117 (2019).

[54] T. Pandey, A. S. Nissimagoudar, A. Mishra, and A. K. Singh, Ultralow thermal conductivity and high thermoelectric figure of merit in mixed valence In_5X_5Br (X= S, and Se) compounds, J. Mater. Chem. A **8**, 13812 (2009).

[55] D. Hobbis, K. Wei, H. Wang, J. Martin and G.S. Nolas, Synthesis, structure, Te alloying and physical properties of $CuSbS_2$, Inorg. Chem. **56**, 140404 (2017).

[56] K. Wei, D. Hobbis, H. Wang and G.S. Nolas, Wittichenite Cu_3BiS_3: Synthesis and physical properties, J. Electronic Mater. **47**, 2374 (2018).

[57] D. Hobbis, H. Wang, J. Martin, and G. S. Nolas, Thermal properties of the very low thermal conductivity ternary chalcogenide $Cu_4Bi_4M_9$ (M = S, Se), Phys. Status Solidi RRL, 8, 2000166 (2020).

[58] R. Hanus, J. George, M. Wood, Y. Cheng, D. L. Abernathy, M. E. Manley, G. Hautier, G. J. Snyder, and R. P. Hermann, Uncovering design principles for amorphous-like heat conduction using two-channel lattice dynamics, Mater. Today Phys. **18**, 100344 (2021).

[59] R. J. Hardy, Energy-flux operator for a lattice, Phys. Rev. **132**, 168 (1963).

[60] P. B. Allen and J. L. Feldman, Thermal conductivity of disordered harmonic solids, Phys. Rev. B **48**, 12581 (1993).

[61] P. B. Allen, J. L. Feldman, J. Fabian, and F. Wooten, Diffusons, locons and propagons: character of atomic vibrations in amorphous Si, Philos. Mag. B **79**, 1715 (2009).

[62] J. Callaway, Model for Lattice Thermal Conductivity at Low Temperatures, Phys. Rev. 113, 1046 (1959).

[63] G. Leibfried, E. Schloemann, Thermal conductivity of dielectric solids by a variational technique, Nachr. Akad. Wiss. Goettingen, Math.-Phys. Kl. 2A: Math.-Phys.-Chem. Abt. 71, 1366 (1954).

[64] P. G. Klemens, The Scattering of Low-Frequency Lattice Waves by Static Imperfections, Proc. Phys. Soc. A68, 1113 (1955).

[65] W. D. C. B. Gunatilleke, N. Alzahrani, A. F. May, H. Wang, and G. S. Nolas, Thermal Properties of the Quaternary Chalcogenide $BaCdSnSe_4$, Phys. Stat. Sol. RRL 14, 2000363 (2020).

[66] G. Chang, B. J. Wieder, F. Schindler, D. S. Sanchez, I. Belopolski, S. Huang, B. Singh, D. Wu, T. Chang, T. Neupert, S. Xu , H. Lin, and M. Z. Hasan, Topological quantum properties of chiral crystals, Nat. Mater. **17**, 978 (2018).

[67] T. Pandey, C. A. Polanco, V. R. Cooper, D. S. Parker, and L. Lindsay, Symmetry-driven phonon chirality and transport in one-dimensional and bulk Ba_3N-derived materials, Phys. Rev. B **98**, 241405 (2018).

[68] L. Lindsay, D. A. Broido, and N. Mingo, Lattice thermal conductivity of single-walled carbon nanotubes: beyond the relaxation time approximation and phonon-phonon scattering selection rules, Phys. Rev. B **80**, 125407 (2009).

[69] M. Christensen, A. B. Abrahamsen, N. B. Christensen, F. Juranyi, N. H. Andersen, K. Lefmann, J. Andreasson, C. R. Bahl, and B. B. Iversen, Avoided crossing of rattler modes in thermoelectric materials, Nat. Mater. **7**, 811 (2008).

[70] W. Li and N. Mingo, Ultralow lattice thermal conductivity of the fully filled skutterudite $YbFe_4Sb_{12}$ due to the flat avoided-crossing filler modes, Phys. Rev. B **91**, 144304 (2015).

Figure Captions

Figure 1. (a) Phonon dispersion of $Ba_6Sn_6Se_{13}$ along high-symmetry directions. The calculated group velocity values are projected as color scale on the dispersion, normalized by the highest calculated velocity value 2883 m/s of an LA mode along the Γ-Y direction. (b) Partial phonon density of states for each atom, with contributions of Sn^{4+} and Sn^{2+} (shaded yellow) differentiated.

Figure 2. Comparison of measured C_p (black) and DFT calculated C_v (blue) (a) normalized, (b) scaled by T^3, and (c) scaled by T with Debye temperatures (θ_D) estimated from the slopes of the linear fits as shown in the figure.

Figure 3. Electron localization function (ELF) of $Ba_6Sn_6Se_{13}$ along various planes intersecting Sn atoms to highlight the differences in electron distribution around the Sn^{2+} and Sn^{4+} species. The center panel highlights a lone pair (red electron density) pointing away from the three bonds this Sn atom shares with neighboring Se atoms.

Figure 4. Measured temperature dependent κ from 4 to 675 K are given by black circles. Modelled temperature dependent κ (red curve) with contributions from phonons divided into two frequency regions, above 4 meV (green curve) and below 4 meV (blue curve), as described in the text.

Figure 5. Low frequency dispersion of $Ba_6Sn_6Se_{13}$ along the (0, 0, z) chiral axis where blue and red indicate different quasiangular momenta l.

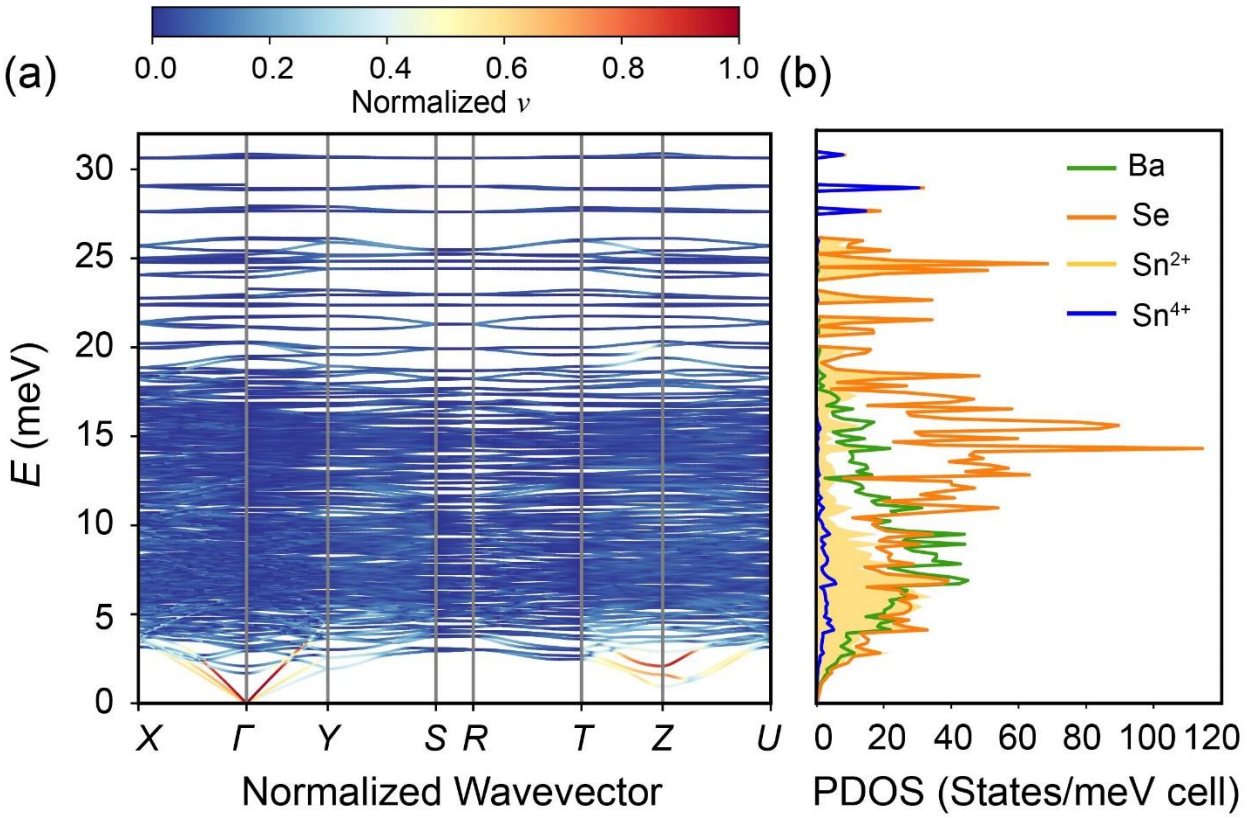
(a)
0.0
0.2
0.4
0.6
0.8
1.0
Normalized v
(b)
30
25
20
15
10
5
0
E (meV)
X
Γ
Y
S
R
T
Z
U
Normalized Wavevector
Ba
Se
Sn^{2+}
Sn^{4+}
0
20
40
60
80
100
120
PDOS (States/meV cell)

Figure 1

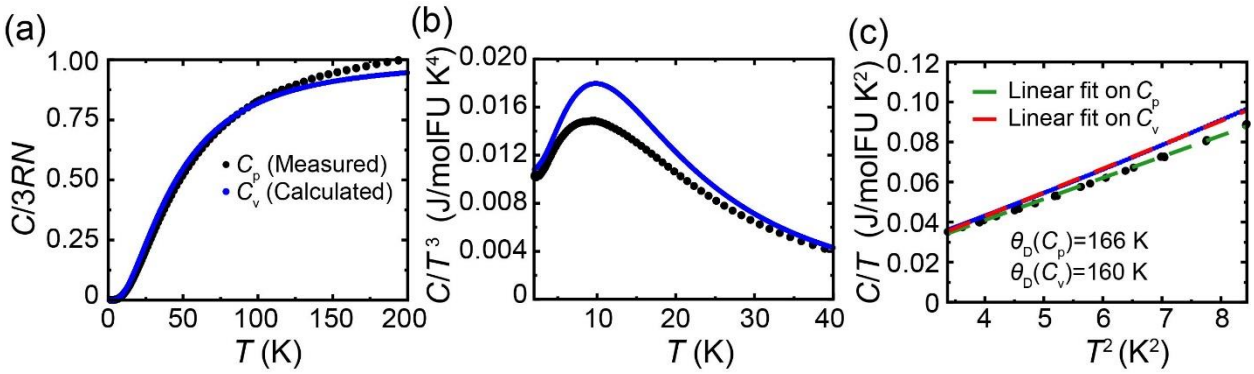
(a)
(b)
(c)
C/3RN
T (K)
C_p (Measured)
C_v (Calculated)
C/T^3 (J/molFU K^4)
C/T (J/molFU K^2)
T^2 (K^2)
Linear fit on C_p
Linear fit on C_v
θ_D(C_p)=166 K
θ_D(C_v)=160 K

Figure 2

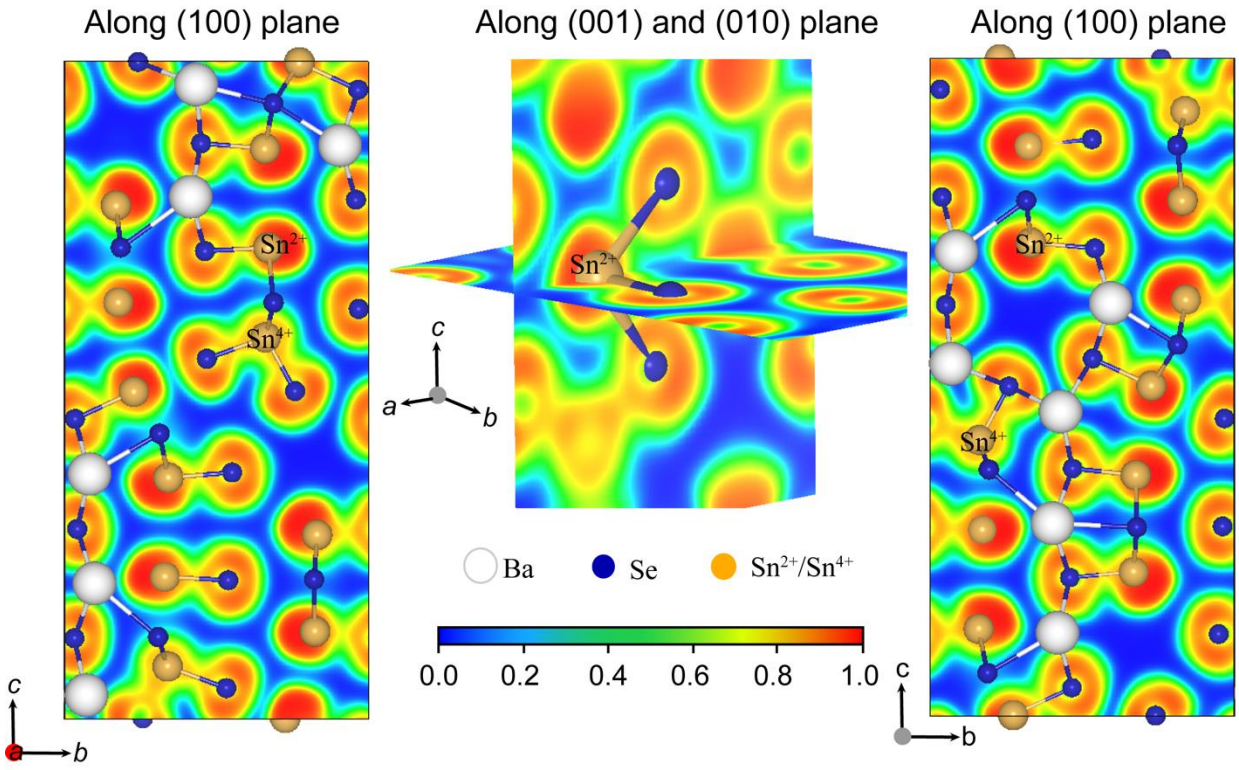
Along (100) plane
Along (001) and (010) plane
Along (100) plane
Sn2+
Sn4+
Sn2+
Sn2+
Sn4+
c
a
b
c
a
b
c
b
Ba
Se
Sn2+/Sn4+
0.0
0.2
0.4
0.6
0.8
1.0

Figure 3

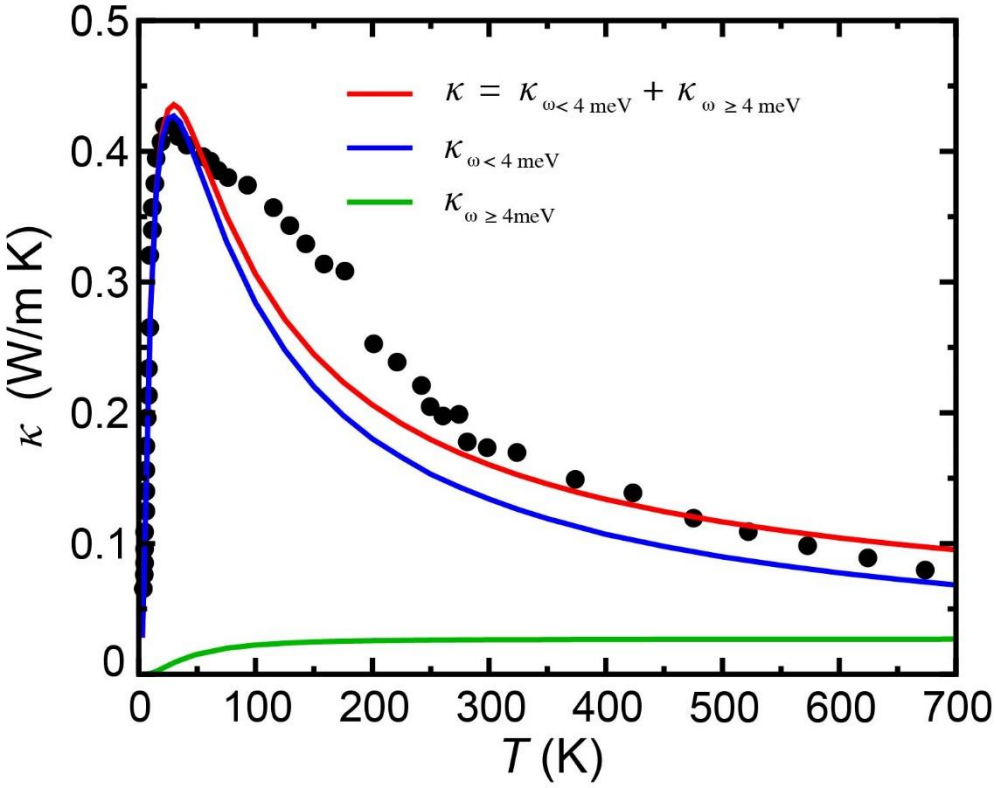
0.5
0.4
0.3
0.2
0.1
0
κ (W/m K)
0
100
200
300
400
500
600
700
T (K)
κ = κ ω< 4 meV + κ ω ≥ 4 meV
κ ω < 4 meV
κ ω ≥ 4meV

Figure 4.

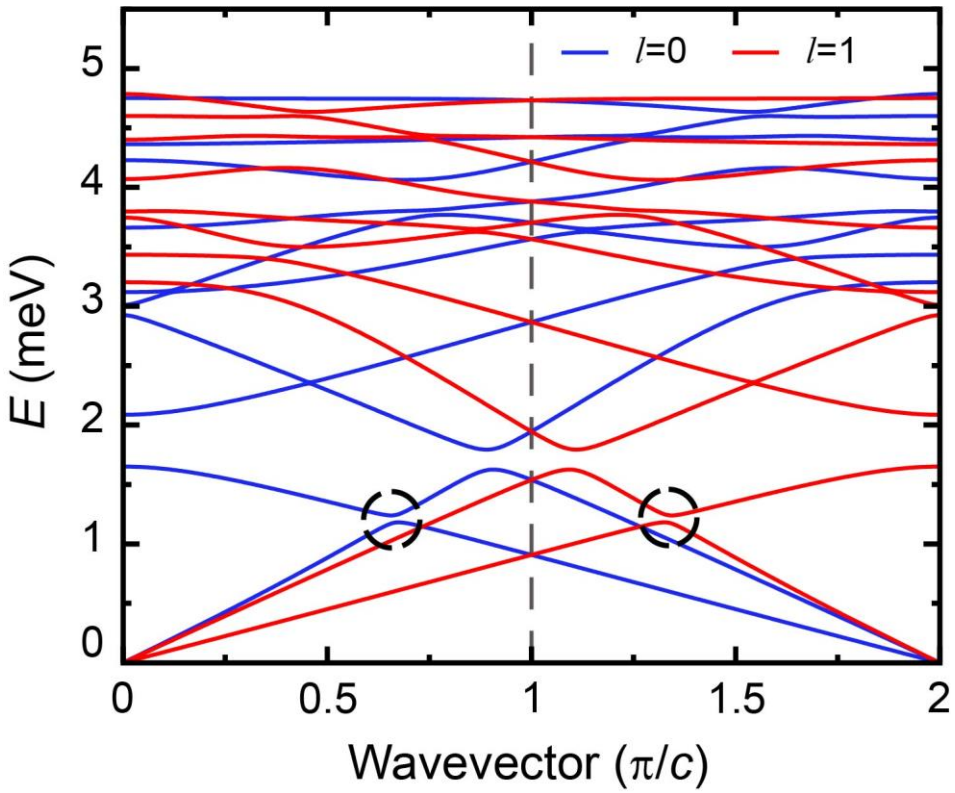

Figure 5